ϕ and ω meson production in pp reactions at $p_{\text{lab}} = 3.67$ GeV/c

F. Balestra,[1] Y. Bedfer,[2,*] R. Bertini,[1,2] L. C. Bland,[3] A. Brenschede,[4,†] F. Brochard,[2,‡] M. P. Bussa,[1] Seonho Choi,[3,§]
M. Debowski,[5] R. Dressler,[6] M. Dzemidzic,[3,‖] J.-Cl. Faivre,[2,*] I. V. Falomkin,[7,¶] L. Fava,[8] L. Ferrero,[1] J. Foryciarz,[9,5,**]
I. Fröhlich,[4] V. Frolov,[7] R. Garfagnini,[1] A. Grasso,[1] E. Grosse,[6] S. Heinz,[1,2] V. V. Ivanov,[7] W. W. Jacobs,[3] W. Kühn,[4]
A. Maggiora,[1] M. Maggiora,[1] A. Manara,[1,2] D. Panzieri,[8] H.-W. Pfaff,[4] G. Piragino,[1] G. B. Pontecorvo,[7] A. Popov,[7]
J. Ritman,[4] P. Salabura,[5] V. Tchalyshev,[7] F. Tosello,[1] S. E. Vigdor,[3] and G. Zosi[1]

(DISTO Collaboration)

[1]*Dipartimento di Fisica "A. Avogadro" and INFN, Torino, Italy*
[2]*Laboratoire National Saturne, CEA Saclay, France*
[3]*Indiana University Cyclotron Facility, Bloomington, Indiana 47408*
[4]*II. Physikalisches Institut, University of Gießen, Germany*
[5]*M. Smoluchowski Institute of Physics, Jagellonian University, Kraków, Poland*
[6]*Forschungszentrum Rossendorf, Germany*
[7]*JINR, Dubna, Russia*
[8]*Universita' del Piemonte Orientale and INFN, Torino, Italy*
[9]*H. Niewodniczanski Institute of Nuclear Physics, Kraków, Poland*

The exclusive production cross sections for ω and ϕ mesons have been measured in proton-proton reactions at $p_{\text{lab}} = 3.67$ GeV/c. The observed ϕ/ω cross section ratio is $(3.8 \pm 0.2^{+1.2}_{-0.9}) \times 10^{-3}$. After phase space corrections, this ratio is enhanced by about an order of magnitude relative to naive predictions based upon the Okubo-Zweig-Iizuka (OZI) rule, in comparison to an enhancement by a factor ~ 3 previously observed at higher beam momenta. The modest increase of this enhancement near the production threshold is compared to the much larger increase of the ϕ/ω ratio observed in specific channels of $\bar{p}p$ annihilation experiments. Furthermore, differential cross section results are also presented which indicate that although the ϕ meson is predominantly produced from a $^3P_1$ proton-proton entrance channel, other partial waves contribute significantly to the production mechanism at this beam momentum.

I. INTRODUCTION

The proton is a complex composite object in which sea-quarks and gluons make significant contribution to the structure functions. Investigation of the strange structure of the nucleon is currently of great interest since strange quarks appear only as sea quarks in most models of the nucleon in contrast to the light quarks (u and d) that appear as both valence and sea quarks.

An important experimental approach to study the role of strange quarks in the proton's wave function is to measure the relative production of ϕ and ω vector mesons. Since the singlet-octet mixing angle of the ground state vector meson nonet is close to the ideal value (i.e., $\tan \theta_{\text{ideal}} = 1/\sqrt{2}$) [1], the ω meson consists almost completely of light valence quarks and the ϕ meson almost completely of strange valence quarks. According to the Okubo-Zweig-Iizuka (OZI) rule, processes with disconnected quark lines in the initial or final state are suppressed [2–5]. As a result, the production of the ϕ meson is expected to be strongly suppressed relative to the ω meson in hadronic reactions with no strange quarks in the initial state. Under the assumption that the OZI rule is exactly fulfilled, the ϕ meson can only be produced by the small admixture of light quarks to its wave function. Thus, the relative production cross sections for the ϕ and ω mesons ($R_{\phi/\omega}$) can be calculated by the following formula:

$$R_{\phi/\omega} = f \times \tan^2 \delta = f \times 4.2 \times 10^{-3}, \tag{1}$$

where f is a correction for the available phase space, and $\delta \approx 3.7°$ is the deviation from the ideal mixing angle [6].

In certain hadronic reactions it has been observed that the ratio of the exclusive cross sections for the ϕ and ω meson production reactions significantly exceeds estimates based on simple quark models (see, e.g. [7]). For $\bar{p}p$ annihilation at rest this enhancement is observed to be particularly dramatic [8–10]. This apparent violation of the OZI rule has been interpreted as evidence for a non-negligible negatively polarized $s\bar{s}$ Fock component to the proton's wave function [7,11]. Here it is important to distinguish between extrinsic and intrinsic quark and gluon contributions to the nucleon sea [12,13], since other explanations stress the importance of higher order rescattering processes [14–19], thereby "avoiding" the OZI rule.

---

*Present address: DAPNIA/SPhN, CEA Saclay, France.

†Present address: Brokat Infosystems AG, Stuttgart, Germany.

‡Present address: LPHNHE, Ecole Polytechnique, 91128 Palaiseau, France.

§Present address: Temple University, Philadelphia, PA 19122.

‖Present address: IU School of Medicine, Indianapolis, IN 46202.

¶Deceased.

**Present address: Motorola Polska Software Center, Kraków, Poland.

Recently, there have been numerous experimental investigations on the contribution of strange quarks to the proton: At low momentum transfers q^2 there are measurements of parity violating polarized electron-proton scattering to determine the strange electromagnetic form factors of the nucleon. First results indicate very small effects [20,21], and thus the scale of the strange vector current $\langle N|\bar{s}\gamma_\mu s|N\rangle$ cannot yet be determined (see, e.g. [22]). Spin dependent structure functions have also been measured in a number of inclusive [23–31] and semi-inclusive [32,33] experiments on deep inelastic scattering of polarized leptons from nucleons, suggesting that the strange sea quarks are weakly polarized against the proton helicity. Furthermore, it has commonly been discussed that the magnitude of the $\Sigma_{\pi N}$ term in low energy pion nucleon elastic scattering [34–37] indicates a possibly sizable, but very uncertain scalar density of strange sea quarks $\langle N|\bar{s}s|N\rangle$ in the nucleon's wave function.

The negatively polarized intrinsic strangeness model was in part motivated by the strong correlation of the ϕ meson yield to the spin triplet fraction of the annihilating $p\bar{p}$ system [38]. Since ϕ meson production in pp reactions at threshold must proceed via the spin triplet entrance channel, further insight on the origin of the enhanced ϕ production in $p\bar{p}$ could be provided by studying near-threshold pp reactions, where predictions based upon the strange sea quarks in the nucleon and meson rescattering models might be expected to differ.

To address this problem we have measured the production of ϕ and ω mesons in proton-proton reactions with the DISTO spectrometer [39] at the Saturne accelerator in Saclay. We present here total and differential cross sections that were determined for a beam momentum of 3.67 GeV/c which corresponds to a much lower available energy above the ϕ production threshold ($Q = \sqrt{s} - \sqrt{s_0} = 83$ MeV) than the existing data ($Q > 1.6$ GeV) [40–43]. In previous letters [44,45] we have presented the first results close to the ϕ meson production threshold in proton-proton reactions, where it was determined that the ϕ/ω cross section ratio increases slightly toward threshold. Since these publications we have made several improvements to the data analysis, including refinements of the acceptance correction, improvements in the tracking algorithm and calibrations, as well as the analysis of a factor four more statistics. These results are presented here in more detail, together with differential cross section distributions that were previously not available. All of the previously published data are consistent with the results presented here.

This paper is organized as follows. In the next section experimental details of the detector and data analysis are presented. The resulting ϕ and ω meson total and differential cross sections are presented in the ensuing section, followed by a discussion of these results and a summary.

II. EXPERIMENT

A. Apparatus

A proton beam from the SATURNE synchrotron with momentum $p_{\text{lab}} = 3.67$ GeV/c was directed onto a liquid hy-
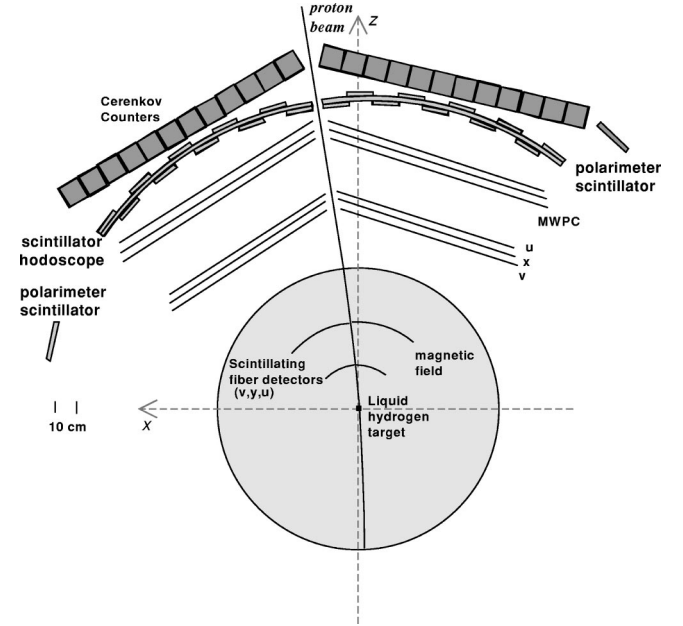

FIG. 1. Schematic layout of the DISTO experimental apparatus, viewed from above. The large shaded area represents the effective field region.

drogen target of 2 cm length, and multiple charge particle final states were measured with the DISTO spectrometer [39], which is shown schematically in Fig. 1. Charged particles were tracked through a magnetic spectrometer and detected by a scintillator hodoscope and an array of water Čerenkov detectors. The magnetic spectrometer consisted of a dipole magnet (1.0 T m), 2 sets of scintillating fiber hodoscopes inside the field, and 2 sets of multiwire proportional chambers (MWPC) outside the field. The large acceptance of the spectrometer ($\approx \pm 15°$ vertical, $\pm 48°$ horizontal) allowed for coincident detection of four charged particles, which was essential for the kinematically complete reconstruction of many final states ($pp\pi^+\pi^-$, $pp\pi^+\pi^-\pi^0$, ppK^+K^-, $pK\Lambda$, $pK\Sigma$). Particle identification and 4-momentum conservation served as powerful tools for background rejection. Event readout was triggered by a multiplicity condition on the scintillating fiber and hodoscope detectors, selecting events with at least three charged particles. Details of the experimental apparatus can be found in Ref. [39].

B. Data analysis

The exclusive reactions $pp \to pp\eta$ and $pp \to pp\omega$ were identified via the $\pi^+\pi^-\pi^0$ decay of the η and ω mesons with partial widths $\Gamma/\Gamma_{\text{tot}} = 0.232$ and $\Gamma/\Gamma_{\text{tot}} = 0.888$, respectively [1]. For the $pp \to pp\phi$ reaction, the ϕ was observed via its K^+K^- decay with $\Gamma/\Gamma_{\text{tot}} = 0.491$. Since these channels all have four charged particles in the final state (three positive and one negative), these events could be reconstructed by applying particle identification and kinematical constraints on an event-by-event basis to the same sample of four track events.

1. Tracking

After calibration, the data from the magnetic spectrometer consist of a collection of points in space determined by the various detector components. Thus, the first major step in the data analysis is to determine the trajectories of the charged particles from the detector position information. In general, a particle's trajectory is defined by five independent parameters. These parameters can be chosen in numerous ways, however they must span the space of allowed possibilities. The choice of track parameters used in this experiment to define the trajectories was motivated by the dipole magnetic field geometry, and was based on a right handed coordinate system with its origin in the center of the target, $\hat{z}$ in the beam direction at the target, and $\hat{y}$ (vertical) along the magnetic field direction. The five track parameters used were X and Y to describe the intersection of the track with the $\hat{x} - \hat{y}$ plane through the origin, ϕ to describe the angle of the track's projection onto the $\hat{x} - \hat{z}$ plane at the point $(X, Y, 0)$, m to describe the ratio of the particle's momentum along $\hat{y}$ to the momentum in the $\hat{x} - \hat{z}$ plane, and p_{xz} for the reciprocal of the momentum in the $\hat{x} - \hat{z}$ plane.

The observed positions in the detectors can be calculated as a function of these five parameters by detailed Monte Carlo simulations of the detector performance. The goal of the tracking algorithm is to invert this function, i.e., determine the track parameters from the measured position information. This is done in a two step procedure: In the first step (track-search) it is determined which hits belong together to form a track. Then, in the track-fit procedure the five track parameters are determined from the hits in an iterative, quasi-Newton procedure by interpolating within a matrix of reference trajectories.

2. Particle identification

Particle identification was achieved using the light output from the water Čerenkov detectors, which provided good π^+-proton separation spanning a wide range of momenta, as well as $K^\pm$ identification in a restricted range above the kaon Čerenkov threshold $p_{K,\text{th}} = M_K c/\sqrt{n^2 - 1}$. Water was chosen as the Čerenkov radiator ($n = 1.33$, $p_{K,\text{th}} = 560$ MeV/c) in order to match the momentum range of the kaons from the reaction $pp \rightarrow pp K^+ K^-$, which are distributed around 700 MeV/c.

The inclusive correlation of Čerenkov amplitude versus momentum is shown in Figs. 2(a) and 2(c) for negatively and positively curved tracks, respectively. These figures have a logarithmic intensity scale with a factor of 2.4 between intensity contours. In Fig. 2(a) there is a clear band from the π^- mesons. The K^- mesons are not visible in this inclusive distribution because of the $\sim 10^5$ larger pion yield. On the other hand, there is already a weak indication of the K^+ mesons in Fig. 2(c) in addition to the prominent π^+ meson and proton lines. The relative yield of a given kaon species can be enhanced by imposing two requirements on the data set: The first is that the oppositely charged meson is consistent with being a kaon, and the second is 4-momentum conservation for the given event hypothesis (i.e. pp
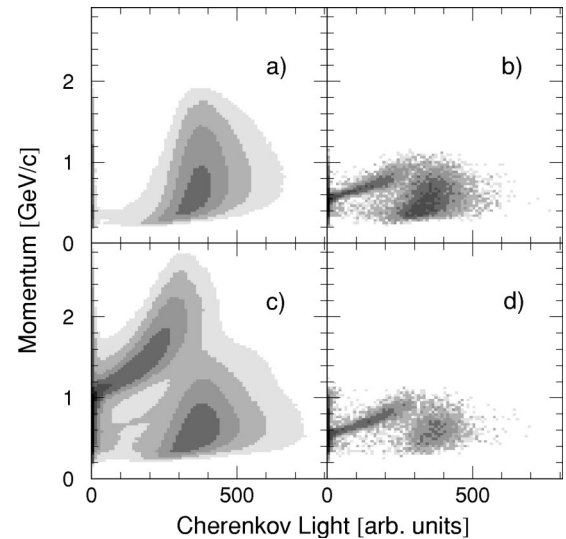

FIG. 2. Plots of the Čerenkov light output versus particle momentum for negatively [(a) and (b)] and positively [(c) and (d)] charged particles. The figures on the left are inclusive distributions and the figures on the right are the same distributions after requiring that the other Čerenkov amplitude is consistent with kaon identification and that the four observed particle momenta are consistent with 4-momentum conservation for the event hypothesis $pp K^+ K^-$.

$\rightarrow pp K^+ K^-$). The remaining yield after imposing these restrictions is shown in Figs. 2(b) and 2(d), where signals from the K^+ and K^- mesons are now clearly visible.

3. Event reconstruction

The data sample analyzed here with four charged particles contained events from many different types of reactions. The individual reactions were identified by a combination of particle identification of the charged particles in the final state and kinematic constraints on the measured particles. The charged particles in the final state, predominantly protons, pions, and kaons, were identified with the water Čerenkov detectors as described above. However, since the same final state could be produced via several reaction channels, kinematic conditions were required to discriminate among the particular reaction channels.

All reaction channels studied here contained at most one unmeasured particle in the final state, thus the measured four track events were kinematically complete. As a result 4-momentum conservation was imposed as a powerful constraint to select events of a given hypothesis. For this the invariant mass and missing mass of various particle configurations were calculated: The invariant mass (M_{inv}) is the total energy in the reference frame of a given number of observed particles. M_{inv} can be calculated from the total energies (E) and momenta ($\vec{p}$) of the n individual particles using the following formula:

$$(M_{\text{inv}})^2 = \left(\sum_{i=1}^{n} E_i \right)^2 - \left(\sum_{i=1}^{n} \vec{p}_i \right)^2. \tag{2}$$

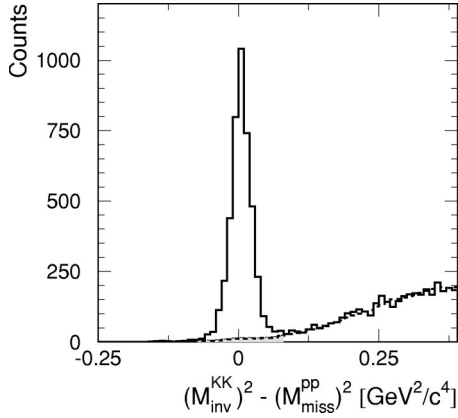The missing mass analysis was used to determine the rest

FIG. 3. Distribution of $(M_{\mathrm{inv}}^{KK})^2 - (M_{\mathrm{miss}}^{pp})^2$ for the event hypothesis $pp \to ppK^+K^-$. The dashed histogram is an estimate of the background by scaling the inclusive distribution without applying kaon Čerenkov requirements.

mass of an unobserved recoil particle. The missing mass (M_{miss}) is given by the following formula:

$$(M_{\mathrm{miss}})^2 = \left(E_{\mathrm{beam}} + M_p - \sum_{i=1}^{m} E_i \right)^2 - \left(\vec{p}_{\mathrm{beam}} - \sum_{i=1}^{m} \vec{p}_i \right)^2, \tag{3}$$

where the index i runs over all m observed particles. The specific application of these constraints is discussed in the following sections.

The results presented here on the production of the ϕ meson were determined by selecting events of the type $pp \to ppK^+K^-$. For this event hypothesis, the proton-proton missing mass (M_{miss}^{pp}) must equal the invariant mass of the kaon pair (M_{inv}^{KK}). Since all four particles in the final state have been measured, the event reconstruction has been performed requiring that the four particle missing mass (M_{miss}^{ppKK}) be equal to zero. The distribution of $(M_{\mathrm{inv}}^{KK})^2 - (M_{\mathrm{miss}}^{pp})^2$ is plotted in Fig. 3 including kaon identification (solid histogram) based on the Čerenkov detectors. The peak at $(M_{\mathrm{inv}}^{KK})^2 - (M_{\mathrm{miss}}^{pp})^2 \approx 0$ results from events consistent with the $pp \to ppK^+K^-$ hypothesis, and is superimposed on a background resulting from imperfect $\pi - K$ separation in the Čerenkov detectors in a small fraction of events of the type $pp \to pK^+\Lambda \to ppK^+\pi^-$ or $pp \to pp\pi^+\pi^-X$. The dashed histogram is an estimate of the background by scaling the inclusive distribution without kaon Čerenkov requirements by a factor 0.002 in order to match the data in Fig. 3 above 0.15 GeV$^2/c^4$. The background from non ppK^+K^- final states comprises only about 2.2% of the yield in the range $|(M_{\mathrm{inv}}^{KK})^2 - (M_{\mathrm{miss}}^{pp})^2| < 0.09$ GeV$^2/c^4$, which marks the range where events were accepted for the further analysis.

The exclusive reaction channel $pp \to pp\omega$ was measured via the $\omega \to \pi^+\pi^-\pi^0$ decay and was selected by a missing mass analysis since the π^0 decays primarily into two photons ($\Gamma_{\gamma\gamma}/\Gamma_{\mathrm{tot}} = 0.988$) which are not detected in the spectrometer. Events of the type $pp\pi^+\pi^-\pi^0$ were selected by first requiring that the Čerenkov amplitudes associated with the four charged tracks be consistent with the hypothesis
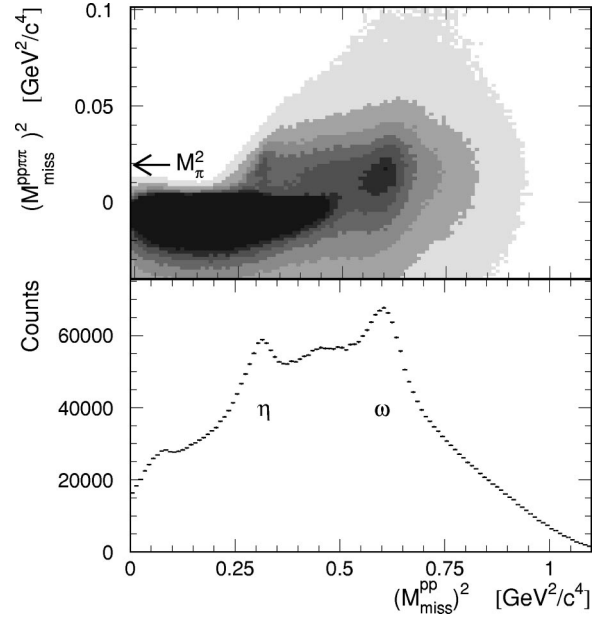

FIG. 4. Distribution of $(M_{\mathrm{miss}}^{pp\pi^+\pi^-})^2$ versus $(M_{\mathrm{miss}}^{pp})^2$ (upper frame). The lower frame shows prominent peaks from the η and ω mesons in the projection onto the $(M_{\mathrm{miss}}^{pp})^2$ axis after requiring $(M_{\mathrm{miss}}^{pp\pi^+\pi^-})^2 \approx (M_\pi)^2$.

$pp\pi^+\pi^-$. Furthermore, background from four body reactions of the type $pp\pi^+\pi^-$ with $M_{\mathrm{miss}}^{pp} \sim M_\omega$ is partially suppressed by requiring the invariant mass of the pion pair to fulfill $(M_{\mathrm{inv}}^{\pi^+\pi^-})^2 < (M_\omega - M_{\pi^0})^2$. After these requirements, the distribution of the four particle missing mass squared $(M_{\mathrm{miss}}^{pp\pi^+\pi^-})^2$ versus the proton-proton missing mass $(M_{\mathrm{miss}}^{pp})^2$ is shown in Fig. 4 with a linear scale for the intensity contours. As seen in this figure, there is a very strong signal for the $pp \to pp\omega \to pp\pi^+\pi^-\pi^0$ reaction at $(M_{\mathrm{miss}}^{pp\pi^+\pi^-})^2 \approx (M_{\pi^0})^2$ and $(M_{\mathrm{miss}}^{pp})^2 \approx (M_\omega)^2$. The projection of this distribution onto the $(M_{\mathrm{miss}}^{pp})^2$ axis is shown in the lower frame of Fig. 4 with the additional requirement that $(M_{\mathrm{miss}}^{pp\pi^+\pi^-})^2 \approx (M_{\pi^0})^2$. In this figure, there are clear peaks from the $\pi^+\pi^-\pi^0$ decay of the η and ω mesons. The structure at very low $(M_{\mathrm{miss}}^{pp})^2$ is due to contamination of four body events of the type $pp\pi^+\pi^-$.

C. Acceptance correction

The relative acceptance of the apparatus for the $pp\eta$, $pp\omega$ and ppK^+K^- production channels has been evaluated by means of Monte Carlo simulations, which after digitization, were processed through the same analysis chain as the measured data. The relative acceptance could be determined independent of the actual phase space distribution of the particles in the final state, because the following two requirements are fulfilled with the DISTO spectrometer: (i) the detector acceptance was determined as a function of all relevant degrees of freedom in the final state, and (ii) after accounting for the azimuthal and reflection symmetries, the detector acceptance was nonzero over the full kinematically allowed region.

TABLE I. Kinematic variables and the number of bins per variable associated with the acceptance correction matrices for the ppK^+K^- final state (matrices A and B), and for the ppX final states, where $X = \eta, \omega$.

Kinematic variable	$(M^{p_1 X}_{\text{inv}})^2$	$(M^{p_2 X}_{\text{inv}})^2$	$\Theta^X_{\text{c.m.}}$	$\phi^X_{\text{c.m.}}$	$\Psi^{pp}_{\text{c.m.}}$	M^{KK}_{inv}	Θ^K_X	ϕ^K_X
Matrix A ($X = K^+K^-$)	4	4	1	1	4	1	10	4
Matrix B ($X = K^+K^-$)	1	1	10	1	4	40	1	1
$pp \to ppX (X = \eta, \omega)$	10	10	20	1	4			

In order to determine the detector acceptance, the relevant degrees of freedom were each subdivided into a specific number of bins, thus defining a multidimensional matrix. Next, the number of both the generated and the reconstructed events from the simulations were stored in separate copies of this matrix. Finally, the bin-by-bin ratio of the number of generated to the number of reconstructed events provided the efficiency correction matrix.

When analyzing the data the acceptance correction procedure was performed on an event-by-event basis by first determining the phase space bin of the particular event and then incrementing the distributions by the corresponding acceptance correction factor from the acceptance correction matrix described below. These correction factors include the appropriate partial widths and the simulations account for the lifetime and different decay modes of all unstable particles involved.

1. ppK^+K^- final state

Although there are in general 16 degrees of freedom for four particles in the final state, numerous constraints exist which significantly lower the total number of independent degrees of freedom. For instance, particle identification and 4-momentum conservation reduce the number of degrees of freedom to 8 for the ppK^+K^- final state. The remaining degrees of freedom can be parameterized in numerous ways, with the only restriction that the variables chosen must span the space of allowed possibilities.

Without loss of generality the eight kinematic degrees of freedom for the ppK^+K^- final state can be parametrized as if the reaction proceeded in two steps, i.e., $pp \to p_1 p_2 X \to p_1 p_2 K^+K^-$. In this case, five variables can be used to describe the three body system ppX, and the remaining three degrees of freedom are then required to uniquely determine the decay of the intermediate state X. This choice of kinematic variables provides a complete basis and does not require that the reaction actually proceeds via the intermediate state X. The ppX system is parametrized by the two invariant mass combinations $(M^{p_1 X}_{\text{inv}})^2$ and $(M^{p_2 X}_{\text{inv}})^2$ (i.e., Dalitz plot variables of the ppX system), and three Euler angles to describe the orientation of the ppX decay plane in the center of mass reference frame (c.m.): the polar and azimuthal angles of the X intermediate state $\Theta^X_{\text{c.m.}}$, $\phi^X_{\text{c.m.}}$, and a rotation of the ppX decay plane around the direction of X, $\psi^{pp}_{\text{c.m.}}$. Furthermore, three variables are required to describe the decay of X: the mass $M_X = M^{KK}_{\text{inv}}$, and the emission angles of one of the kaons in the X reference frame Θ^K_X and ϕ^K_X where these

angles are measured relative to the beam direction.[1] The beam direction is chosen as the reference direction for the X decay to facilitate comparison in Sec. III B with simple expectations for ϕ-meson decay when it is produced near threshold in pp reactions.

The differential cross section for X production must be isotropic as a function of the azimuthal angle $\phi^X_{\text{c.m.}}$. Therefore, in the simulations $\phi^X_{\text{c.m.}}$ has been integrated with an isotropic distribution to determine the detector acceptance as a function of the remaining seven degrees of freedom.

Due to the high dimensionality of this problem, even a small number of bins per kinematic variable result in an acceptance correction matrix that is too large to calculate with the available computational facilities. For a subdivision of each degree of freedom into $N = 10$ bins, and an average of $M = 20\,000$ events simulated per bin of the acceptance matrix, a total of $M \times N^7 \approx 2 \times 10^{11}$ would have to be simulated. Thus, in order to explore the dependence of the detector acceptance on the remaining seven kinematic variables, two subsets of the general acceptance correction matrix (matrix A and matrix B) have been generated by integrating over several of the kinematic variables as discussed below and summarized in Table I.

The simulations for matrix A contain two simplifications in order to make the calculations tractable. The first simplification is the requirement that the mass of the intermediate state X be equal to the ϕ meson mass. Of course this requirement restricts the use of matrix A to the $pp\phi$ reaction only; however, little systematic error is introduced because the shape of the mass distribution of the ϕ meson is well known and the detector acceptance varies little over it. Furthermore, an isotropic angular distribution of the differential cross section for ϕ meson production versus $\Theta^\phi_{\text{c.m.}}$ has been assumed for matrix A. This assumption is consistent with the observation that this angular distribution turns out to be isotropic when matrix B (see below), which includes explicitly the $\Theta^X_{\text{c.m.}}$ dependence, is used for the acceptance correction. Therefore, in the simulations to calculate matrix A, the inter-

---

[1]The following conventions are used to label the various angles that appear in this report: Θ corresponds to polar angles measured with respect to the beam axis, and Ψ corresponds to polar angles measured with respect to any other quantization axis, which will be explicitly stated. Azimuthal angles are labeled by ϕ and ψ, respectively. The subscript denotes the reference frame in which the angle in measured, and the superscript denotes the particle being measured.

mediate state X was given the ϕ meson mass and the angular variables $\Theta^X_{\text{c.m.}}$ and $\phi^X_{\text{c.m.}}$ were integrated over with isotropic distributions when determining the acceptance as a function of the remaining five variables.

In order to overcome the restrictions on the usage of the acceptance correction matrix A mentioned above, the available degrees of freedom in the ppK^+K^- final state were subdivided differently, as listed in Table I, resulting in the acceptance correction matrix B. Here the variables M^{KK}_{inv} and $\Theta^X_{\text{c.m.}}$ were explicitly included in matrix B. However, an isotropic distribution for the decay $X \to K^+K^-$ was used in order to reduce the dimensionality of the matrix to a solvable level. The validity of using an isotropic decay of $X \to K^+K^-$ can be judged by the data presented in Sec. III B using matrix A. Furthermore, the variables $(M^{p_1X}_{\text{inv}})^2$ and $(M^{p_2X}_{\text{inv}})^2$ were integrated over with a weighting according to three body phase space. This was motivated by the observation that the physical distributions show only small deviations from isotropy and double checked to give consistent results with a different generator for the ppX system.

2. $pp\,\pi^+\pi^-\pi^0$ final state

For the measurements of the η and ω meson production there are five particles in the final state of each channel observed. The 20 degrees of freedom associated with five particles are reduced to 12 because of 4-momentum conservation and four particles have been identified. Two further degrees of freedom are eliminated by requiring $M^{pp}_{\text{miss}} = M_{\eta,\omega}$, respectively, and $M^{pp\pi^+\pi^-}_{\text{miss}} = M_{\pi^0}$. Of the remaining 10 degrees of freedom, five are related to the ppX system where $X = \eta, \omega$ and five to the corresponding decay $X \to \pi^+\pi^-\pi^0$.

The ppX system is parametrized by the Dalitz plot variables $(M^{p_1X}_{\text{inv}})^2$ and $(M^{p_2X}_{\text{inv}})^2$, as well as three Euler angles to describe the orientation of the ppX decay plane: $\Theta^X_{\text{c.m.}}$, $\phi^X_{\text{c.m.}}$, and $\psi^{pp}_{\text{c.m.}}$. As discussed above, the differential cross section is isotropic in $\phi^X_{\text{c.m.}}$, thus there are in effect four independent degrees of freedom plus those associated with the decay of the meson X. The matrix element associated with the $\omega \to \pi^+\pi^-\pi^0$ decay was taken from [46] and verified to be consistent with the data from [47,48], thus allowing the corresponding variables to be integrated over. The matrix element for the η decay was taken from [49–51]. Furthermore, we have assumed an isotropic orientation of the ω decay plane, which was verified to be consistent with the data. Thus, four dimensional efficiency matrices were calculated for the η and ω production reactions, as summarized in Table I.

Although all bins that are kinematically allowed have a finite acceptance, there are some phase space bins with very low acceptance. These bins are associated with backward emission of the η or ω meson (in the c.m. frame). Because the initial system involves two identical particles, the physical distribution must have a symmetry about $\Theta^X_{\text{c.m.}} = 90°$. Thus, in order to reduce the systematic error associated with the very large acceptance corrections at backward angles, all integrated cross section results for the η and ω meson pro-
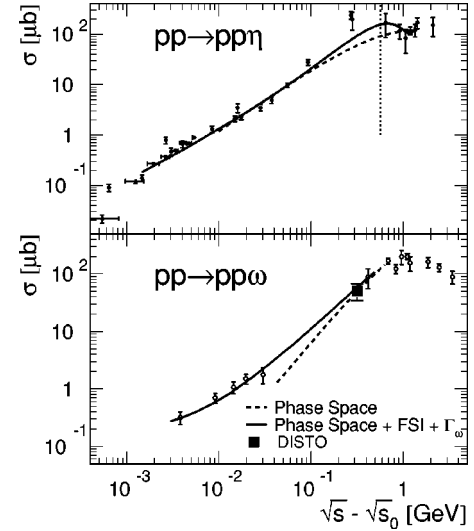

FIG. 5. Exclusive cross section as a function of the total c.m. energy above threshold for the reaction $pp \to pp\,\eta$ (upper frame) and of the reaction $pp \to pp\,\omega$ (lower frame). The data points are referenced in the text. The solid and dashed curves in the upper frame are parametrizations of the data in order to estimate the η meson production cross section at the energy in this experiment, which is marked by the vertical dotted line. The filled square in the lower frame is the result of this experiment. In the lower frame the dashed curve shows the c.m. energy dependence of the three-body $(pp\omega)$ phase space volume. The solid curve additionally includes the finite width of the ω meson and the proton-proton final state interaction (FSI).

duction were calculated for the forward hemisphere only (and then multiplied by two). The differential cross sections however could be extended to backward angles, up to the limits of where the acceptance correction method remained valid, thereby providing an additional check of the calculations.

D. Absolute normalization

The absolute cross section normalization was determined by measuring the yield of a given channel relative to that of a *simultaneously* measured channel with known cross section. This method to determine the absolute normalization was chosen because it reduced the large systematic uncertainty associated with the absolute calibrations of both beam intensity and trigger efficiency. For this work the reference channel was the reaction $pp \to pp\,\eta$, for which a large amount of existing data [52–63] are summarized in the upper frame of Fig. 5.

In order to provide the absolute cross section calibration, the existing published data were interpolated to estimate the η production cross section at the beam momentum of the present measurement. The solid and dashed curves presented in the upper frame of Fig. 5 correspond to two different parametrizations of the measured cross section values. The solid curve corresponds to a polynomial of sixth order and the dashed curve corresponds to a parametrization of the following form:

TABLE II. List of systematic error sources and their effect for the various measured particle ratios.

Systematic error	ϕ/ω	ω/η	K^+K^-/η	ϕ/η
Acceptance correction	5%	5%	5%	5%
ω background	15%	15%		
η background		15%	15%	15%
ϕ background	15%			15%
Trigger bias	10%		10%	10%
Tracking efficiency	10%	10%	10%	10%
Drift in electronics	10%	10%	10%	10%
K^+K^- identification	10%		10%	10%
$\pi^+\pi^-$ identification	10%	5%	10%	10%
Total	32%	27%	27%	32%

$$\sigma_{pp\to pp\eta}=a\left(\frac{s}{s_0}-1\right)^b\left(\frac{s_0}{s}\right)^c, \qquad (4)$$

where $\sqrt{s_0}=(2M_p+M_\eta)$ is the c.m. energy at the η meson production threshold, and a,b and c are free parameters. The vertical dotted line marks the available energy ($Q=0.554$ GeV) of this measurement.

Both parametrizations describe the existing η total cross section data well with the exception of the measurement at $p_{\text{beam}}=2.8$ GeV/c by Pickup *et al.* [56], which is underestimated. In the upper frame of Fig. 5, both values cited in Ref. [56], for identification via the $\eta\to\pi^+\pi^-\pi^0$ and $\eta\to neutrals$ decay channels are plotted at the corresponding c.m. energy above threshold $Q=0.275$ GeV. This discrepancy has been neglected since that measurement [56] is subject to a large systematic error associated with a quite substantial background subtraction. The average of these two interpolations at $Q=0.554$ GeV is our estimate of 135 ±35 μb for the total cross section of the reaction $pp\to pp\eta$ at our beam momentum. The systematic error from the absolute normalization ($\pm26\%$) is determined from the range of the parameterizations and is similar to or smaller than the systematic error from the combination of all other sources (i.e., 32% for the ϕ/η ratio, see Table II). Furthermore, our estimate is in good agreement with one boson exchange model calculations by Vetter *et al.* [64], who predict ≈120 μb at this energy.

E. Systematic errors

Due to the large amount of data collected, the statistical errors are relatively small, and the experimental error is dominated by systematic uncertainty and systematic bias. This section summarizes the effects studied to estimate the magnitude of the systematic uncertainty, as well as systematic deficiencies of the acceptance correction method and trigger bias.

Systematic uncertainty of the results quoted here have been studied in detail for the following effects.

For the acceptance corrections, the statistical uncertainty of the simulations has been studied by comparing the reconstructed particle ratios using acceptance correction matrices based on different subsets of the simulated data. Further-

more, effects due to the finite binning of the kinematic variables, as well as the finite detector resolution have been considered. Moreover, an additional cross check of the acceptance corrections was provided by the observation that the total ϕ meson yield is identical (within the error range) when determined using both acceptance correction matrices A and B.

A significant source of uncertainty is related to the meson yield determination (back- ground subtraction and peak shape parametrization). This effect was studied by varying the parametrization of the line shapes and background, as well as by varying the fit ranges.

The four track trigger used to record the data presented here had a slightly different efficiency for $pp\pi^+\pi^-$ and ppK^+K^- events. Although this effect has been corrected for, as discussed below, effects such as noise and cross talk in the multianode photomultipliers used for readout of the scintillating fiber detectors introduce an uncertainty to the magnitude of this correction, which we denote as ''trigger bias.''

Similarly, the tracking efficiency of the data analysis procedure may vary slightly between measured and simulated data, primarily due to uncertainty of the actual wire chamber efficiency. In particular, the single track efficiency and correlated efficiency losses due to small spatial separation between tracks have been studied in detail.

Since the data presented here were collected over an extended period of time, residual efficiency losses due to long term drifts in the calibration of the electronics may remain. This effect was examined by comparing the reconstructed particle ratios in temporally separated subsets of the data.

Finally, uncertainty arising from the particle identification in the Čerenkov detectors and the kinematic conditions has been estimated by comparing the efficiency loss due to each individual restriction between the simulated and the measured data.

These results are summarized in Table II. The total systematic uncertainty quoted is determined by quadratically adding the individual terms applicable for a given measured cross section ratio.

In addition to the systematic uncertainty, several effects lead to a systematic bias of the calculated cross section ratios. To estimate the magnitude of the systematic bias we

TABLE III. List of systematic biases and their effect for the various measured particle ratios.

Systematic bias	ϕ/ω	ω/η	ϕ/η
Nontarget events	1.05	1.00	1.05
Trigger bias	0.93	1.00	0.93
ϕ identification	1.07	-	1.07
ω identification	0.93	1.08	
η identification		0.94	0.94
Total	0.97	1.02	0.98

TABLE IV. Ratios of the total meson production cross sections for various reaction combinations including the corresponding statistical and systematic uncertainties. N.B., the values and errors corresponding to the ϕ/η and ϕ/ω ratios have been multiplied by 10^3.

	Ratio	Statistical error	Systematic error
ω/η	0.37	± 0.02	$+0.1 - 0.08$
$\phi/\eta \times 10^3$	1.42	± 0.1	$+0.45 - 0.34$
$\phi/\omega \times 10^3$	3.8	± 0.2	$+1.2 - 0.9$

have examined the following effects.

The liquid hydrogen target was contained in a vessel in which background reactions were produced. These ''nontarget'' events could be well separated by the vertex location in those events with complete scintillating fiber information. Since this separation was not possible in the remaining $\approx 50\%$ of the events, the relative contamination determined in those events with full fiber information was subtracted from the complete data sample.

The data collection trigger required that three of the four charged particles must be observed in the scintillating fiber detectors. Since the fiber detectors had a different response for minimum ionizing pions compared to kaons, which were slower, the trigger efficiency was higher for ppK^+K^- events than for $pp\pi^+\pi^-$ events. The variation of the fiber efficiency has been studied as a function of particle velocity. The magnitude of the trigger bias was thus determined by combining the average kaon and pion efficiencies with the ''three of four'' trigger condition and an estimate of the cross talk in the fiber detectors.

Finally, in the data analysis, conditions were placed on the Čerenkov amplitude of the individual tracks, as well as on several kinematical quantities. The efficiency with which a particular event type is accepted by all these conditions is strongly related to the detector resolution, which may be imperfectly modeled in the simulations, leading to a bias in the efficiency correction matrices. The magnitude of this effect was examined for each meson production reaction by comparing the acceptance loss from each individual selection criterion in the data to the simulations.

The individual contributions to the systematic bias are summarized in Table III as the factor by which they modify the given particle cross section ratio. Based on these considerations, the reconstructed ϕ/ω, ϕ/η, and ω/η cross section ratios have been multiplied by the factors 0.97, 0.98, and 1.02, respectively, to account for the systematic bias. The correction factor for the total K^+K^-/η cross section ratio is the same as for the ϕ/η ratio.

III. RESULTS

After full acceptance corrections, the relative yields for exclusive $\eta, \omega,$ and ϕ meson production in proton-proton reactions at 3.67 GeV/c have been determined. These results are summarized in Table IV, including the statistical and systematic error, and have been combined with the ab-

solute η meson production cross section (see Sec. II D) to determine the absolute cross section results presented below.

A. ω meson production

Using the η meson yield as the absolute normalization, as discussed above, the total cross section for the reaction $pp \rightarrow pp\omega$ is determined to be $(50 \pm 3 ^{+18}_{-16})$ μb with the statistical and systematical error, respectively. This value is plotted as the solid point in the lower frame of Fig. 5. The other data points are from Refs. [58–63,65].

The dashed curve shows the energy dependence according to three-body ($pp\omega$) phase space and has been normalized to the point directly above this measurement (i.e., $\sqrt{s} - \sqrt{s_0} = 0.41$ GeV). The solid curve shows the expected behavior when taking into account the finite width of the ω meson and the proton-proton final state interaction (FSI) [66,67]. Although the energy of this experiment is sufficiently high that pure S wave production is not expected, a smooth variation of the cross section with $\sqrt{s}$ is expected since there are no known baryonic resonances with significant branching ratios to $p\omega$. Thus, the good agreement of the total cross section for ω meson production determined here with the curves in the figure, is a strong indication that the absolute normalization used here does not introduce an error larger than the quoted systematic error. Furthermore, our result is in good agreement with the value (45 ± 7) μb determined in [67] by an interpolation between the existing data.

The differential cross-section for ω meson production has been plotted versus $\cos\Theta_{c.m.}^\omega$ in Fig. 6. This distribution has been fit with the sum of the first three even Legendre poly-
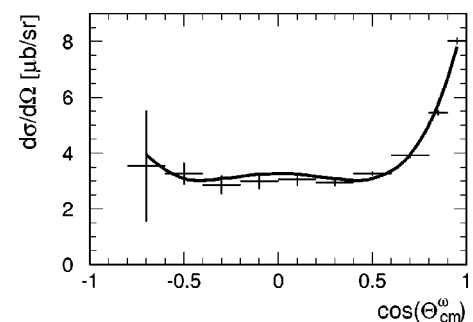

FIG. 6. Differential cross section (in the c.m. frame) for the $pp \rightarrow pp\omega$ reaction as a function of $\cos\Theta_{c.m.}^\omega$. The solid curve is a fit to the data with the sum of the first three even Legendre polynomials.
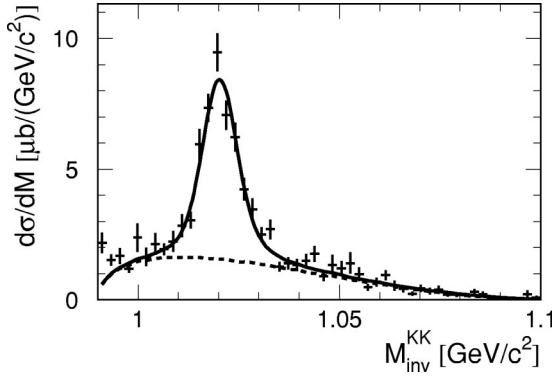
FIG. 7. Acceptance corrected M_{inv}^{KK} distribution. The dashed curve is an estimate of the nonresonant contribution, and is based on the M_{inv}^{KK} dependence of four body phase space ($ppKK$). The solid curve is the sum of the nonresonant and the ϕ meson contributions.

nomials P_i. The best fit has been obtained with the expression below and shown as the solid curve in the figure:

$$\frac{d\sigma}{d\Omega} = (4.0 \pm 0.1)P_0 + (3.1 \pm 0.2)P_2$$

$$+ (2.0 \pm 0.2)P_4 \quad (\mu b/sr). \quad (5)$$

Due to the symmetry of the incoming channel, this angular distribution must have a reflection symmetry about $\cos\Theta_{c.m.}^{\omega} = 0$. Despite the strong variation of the detector acceptance with $\Theta_{c.m.}^{\omega}$, this symmetry is observed in the data, providing a very important confirmation of the validity of the detector acceptance correction method. The deviations from isotropy indicate that partial waves up to $L=2$ for the ω meson relative to the pp system are involved in the production mechanism. Further information such as from polarization degrees of freedom are however required in order to make a quantitative measure of the relative partial wave amplitudes.

B. ϕ meson production

The M_{inv}^{KK} distribution is shown in Fig. 7 after application of the acceptance correction matrix B (which explicitly includes M_{inv}^{KK}) and the absolute normalization discussed above. This distribution has been analyzed to determine what fraction of the yield is due to nonresonant K^+K^- production and what fraction has been produced via the ϕ resonance. The dashed curve shows the estimated nonresonant contribution. The shape of this contribution is given by the M_{inv}^{KK} distribution for final states distributed according to four particle phase space (ppK^+K^-). The shape of the resonant contribution is given by the natural line shape of the ϕ meson folded with a Gaussian to account for the detector resolution. The width of this Gaussian is $\sigma = 3.3 \pm 0.5$ MeV, in good agreement with the simulations ($\sigma = 3.4 \pm 0.1$ MeV). The total cross section for the $pp \rightarrow ppK^+K^-$ reaction, as well as the resonant and nonresonant contributions are summarized in Table V. In addition, the total cross section for ϕ meson

TABLE V. Total production cross section for the reaction $pp \rightarrow ppK^+K^-$ at 3.67 GeV/c and for the resonant (ϕ meson) and nonresonant contributions, together with the statistical and systematic error, respectively.

Production channel	Cross section [μb]
Nonresonant K^+K^-	$0.11 \pm 0.009 \pm 0.046$
$\phi \rightarrow K^+K^-$	$0.09 \pm 0.007 \pm 0.04$
Total K^+K^-	$0.20 \pm 0.011 \pm 0.08$
$(\phi \rightarrow K^+K^-) \times \Gamma_{tot}/\Gamma_{K^+K^-}$	$0.19 \pm 0.014 \pm 0.08$

production has been included after correcting for the branching ratio ($\Gamma_{K^+K^-}/\Gamma_{tot} = 0.491$) and rounding to two significant digits.

The $pp\phi$ final state can be defined by two angular momenta, l_1 is the orbital angular momentum of the two nucleons relative to each other and l_2 is the orbital momentum of the ϕ meson relative to the two nucleon c.m. system. At threshold the $pp\phi$ final state has the orbital angular momenta $l_1 = l_2 = 0$.

The differential cross section for ϕ meson production is plotted versus $\cos\Theta_{c.m.}^{\phi}$ in Fig. 8. This distribution must be symmetric around $\cos\Theta_{c.m.}^{\phi} = 0$. The fact that the observed distribution is indeed symmetric about $\cos\Theta_{c.m.}^{\phi} = 0$ (within the error bars), as it was already observed in Fig. 6 for the angular distribution for the ω meson, is an additional consistency check for the validity of the acceptance corrections. Furthermore, no significant deviations from isotropy are seen in these data, indicating that the ϕ is predominantly in an S wave state relative to the two protons (i.e., $l_2 = 0$). This observation is in good agreement with the expectations of Rekalo $et\ al.$ [68] who claim $l_2 = 0$ up to a ϕ meson c.m. momentum of $p_{\phi}^* \leq M_K c$ which corresponds to an available energy $Q \approx 178$ MeV (in comparison, this measurement is at $Q = 83$ MeV).

Moreover, Rekalo suggests that the pp system may be excited to higher partial waves at much smaller energies above threshold than needed to excite the ϕ meson relative to the protons (i.e., $l_1 = 1, l_2 = 0$ should occur at lower energies than $l_1 = 0, l_2 = 1$). To test this expectation the proton-proton angular distribution has been evaluated for the events with ϕ meson production. In the upper frame of Fig. 9, the differential cross section is plotted as a function of the polar
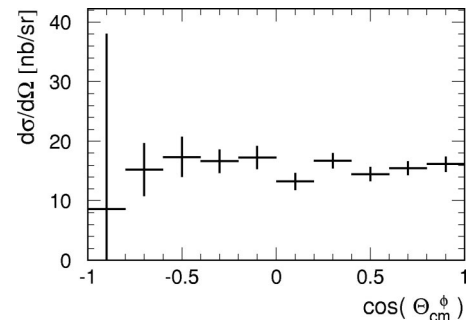

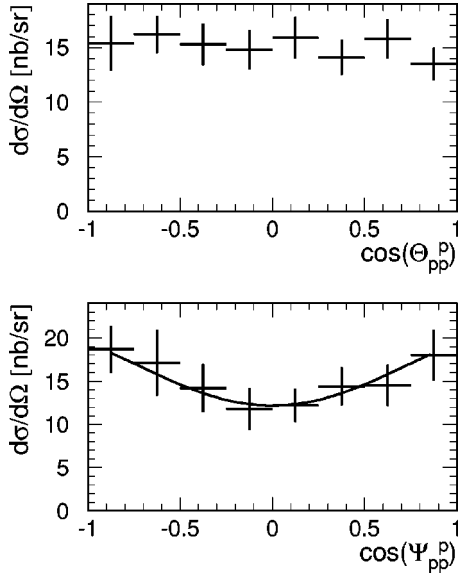FIG. 8. Differential cross section for ϕ meson production as a function of $\cos\Theta_{c.m.}^{\phi}$.

FIG. 9. (Upper frame) Differential cross section for the $pp \rightarrow pp\phi$ reaction plotted as a function of $\cos\Theta_{pp}^p$, measured in the pp reference frame relative to the beam direction. (Lower frame) Differential cross section for the $pp \rightarrow pp\phi$ reaction plotted as a function of $\cos\Psi_{pp}^p$, measured in the pp reference frame relative to the direction of the ϕ meson. The solid line is a fit to the data with the sum of the first three even Legendre polynomials.

angle under which the protons are emitted relative to the beam, measured in the proton-proton reference frame. Here, the observed angular distribution is consistent with being isotropic. On the other hand, the proton-proton angular distribution exhibits a significant deviation from isotropy, when measured relative to the direction of the ϕ meson, as presented in the lower frame of Fig. 9. This distribution has been parametrized with the sum of the first three even Legendre polynomials as listed below and shown as the solid curve in the figure:

$$\frac{d\sigma}{d\Omega} = (15.0 \pm 0.9)P_0 + (5.1 \pm 2.2)P_2$$

$$- (0.7 \pm 3.6)P_4 \quad (\text{nb/sr}). \tag{6}$$

Odd Legendre polynomials have been omitted due to the reflection symmetry of the final pp state about its c.m. motion direction, which is opposite the ϕ momentum in the overall c.m. frame. These data are well described by using only the lowest two Legendre polynomials, as evident by the large uncertainty associated with the P_4 coefficient. These results indicate that partial waves up to $l_1 = 1$ are involved in the proton-proton exit channel.

The momentum distribution of the particles in the final state is also related to the relative partial wave contributions in the $pp\phi$ system. Defining p to be the momentum of a proton in the pp reference frame and q to be the c.m. momentum of the ϕ meson, the total cross section can be written as the sum of the individual partial wave contributions [69]:
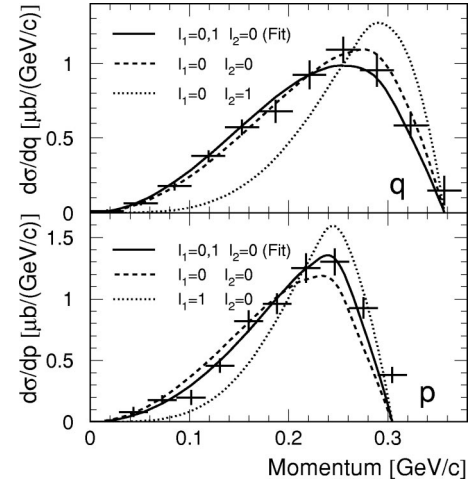

FIG. 10. Differential cross section for the $pp\phi$ reaction as a function of the c.m. momentum q of the ϕ meson (upper frame), and as a function of the proton momentum p in the pp reference frame (lower frame). The dashed curves denote the behavior of the three body phase space when the ϕ meson is in a Ss wave state (i.e., $l_1 = l_2 = 0$) relative to the protons. The dotted curves correspond to the phase space distribution for $l_1 = 0$, $l_2 = 1$ (upper frame) and for $l_1 = 1$, $l_2 = 0$ (lower frame). The solid lines represent a simultaneous fit to both sets of data presented here with the combination of S and P wave contributions in the pp exit channel.

$$\sigma \sim \sum_{l_1, l_2} \int |M_{l_1, l_2}|^2 d\rho_{l_1 l_2}. \tag{7}$$

Here M_{l_1, l_2} is the matrix element for a given final state with angular momenta l_1, l_2, and $d\rho_{l_1 l_2}$ is an element of the three body phase space which is given by the following formulas:

$$d\rho_{l_1 l_2} \sim p^{2l_1 + 1} q^{2l_2 + 2} dq, \tag{8}$$

where the proton momentum is given by

$$p = \sqrt{q_{max}^2 - q^2} \times \sqrt{\frac{1}{4} + \frac{m_p}{2m_\phi}}, \tag{9}$$

and the maximum c.m. momentum of the ϕ meson and the available energy are

$$q_{max} = \sqrt{\frac{4m_p m_\phi Q}{m_\phi + 2m_p}}, \quad Q = \sqrt{s} - \sqrt{s_0}. \tag{10}$$

Assuming that the matrix elements have little variation across the available phase space, then the expected differential cross sections as a function of q and p are proportional to the variation of the three body phase space with q and p. To illustrate this, the ϕ meson differential cross section is plotted in the top frame of Fig. 10 as a function of q. The dashed curve shows the q dependence of the three body phase space for $l_1 = l_2 = 0$, which was normalized to give the smallest χ^2 relative to the measured data. This curve describes the data well. In contrast, the first moment of the dotted curve which denotes the case where the ϕ meson is in a P wave relative

to the nucleons ($l_1 = 0$, $l_2 = 1$) is significantly higher than for the data. These results are consistent with the observation from the data of Fig. 8 that the ϕ meson is in a nearly pure S wave state relative to the protons.

Although the $l_1 = l_2 = 0$ case describes the data well, a slightly better description of the data is generated by including P wave contributions in the proton-proton system (i.e., $l_1 = 0, 1$ and $l_2 = 0$). The relative contributions of $l_1 = 0$ and $l_1 = 1$ has been determined by a combined fit (solid curve) to the data in the top frame of Fig. 10 together with the differential cross section as a function of p, which is shown in the lower frame of Fig. 10. The dashed curve in Fig. 10 denotes the behavior of three body phase space for $l_1 = l_2 = 0$. In this case the data appear to have a significantly higher first moment of p, and as a result, the best description of the data includes a P wave contribution in the pp system. A simultaneous fit to the $d\sigma/dp$ and $d\sigma/dq$ data (solid curve) yields the following ratio of the mean matrix elements for the $l_1 = 1$, $l_2 = 0$ to the $l_1 = l_2 = 0$ states:

$$\frac{|M_{10}|^2}{|M_{00}|^2 + |M_{10}|^2} = 0.28 \pm 0.07. \qquad (11)$$

Further confirmation that higher partial waves are involved in ϕ meson production at this beam momentum can be taken from the angular distribution of the daughter kaons from ϕ meson decay. At threshold (i.e., $l_1 = l_2 = 0$) the Pauli principle requires the outgoing protons to be in a $^1S_0$ state, and thus the total angular momentum and parity of the system must be $J^\pi = 1^-$. In this case, angular momentum and parity conservation require the pp entrance channel to be in a $^3P_1$ state. Since the orbital projection along the beam direction $m_L = 0$ for the incident plane wave, the angular momentum coupling coefficients require the incident pp spin, and hence the outgoing ϕ meson spin, to be aligned along the beam axis [7,19,68]. Consequently, the angular distribution of the daughter kaons in the ϕ meson reference frame must display a $\sin^2\Theta_\phi^K$ distribution relative to the beam direction. At finite energies above threshold the spin alignment of the ϕ meson is diluted by contributions from higher partial waves, thereby modifying the expected angular distribution of the daughter kaons.

The ϕ meson spin alignment can be quantified by the spin density matrix. The elements of the spin density matrix are related to the emission angles of the kaons from the ϕ meson decay. After integrating over the azimuthal emission angle (ϕ_ϕ^K) and imposing $\rho_{11} = \rho_{-1-1}$ and $\rho_{11} + \rho_{00} + \rho_{-1-1} = 1.0$, the diagonal elements of the spin density matrix are related by the following formula to the angular distribution of the daughter kaons (see, e.g. [19]):

$$W(\Theta_\phi^K) = \frac{3}{2}[\rho_{11} \sin^2\Theta_\phi^K + \rho_{00} \cos^2\Theta_\phi^K]. \qquad (12)$$

The differential cross section for the $pp \to pp\phi$ reaction has been evaluated and is presented in Fig. 11 as a function of $\cos\Theta_\phi^K$, based on acceptance matrix A described in Table I. The dotted curve in this figure represents an isotropic dis-
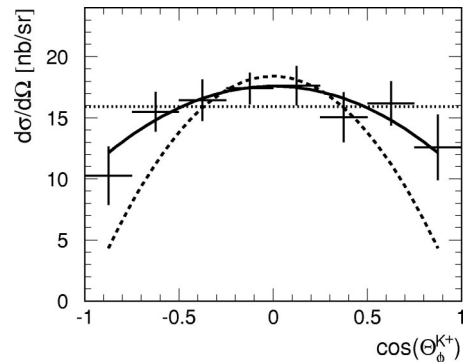

FIG. 11. Differential cross section for the $pp\phi$ reaction plotted as a function of the cosine of the polar angle of the daughter K^+ mesons measured in the ϕ meson reference frame, relative to the beam direction. The curves represent different assumptions for the ϕ meson spin alignment along the beam axis: zero alignment (dotted), full alignment as expected at threshold (dashed), and a fit to the data based on partial alignment (solid).

tribution and the dashed curve corresponds to a $\sin^2\Theta_\phi^K$ distribution, which is the expected behavior at threshold due to the complete alignment of the ϕ meson spin (i.e., $\rho_{00} = 0.0$). Within the statistical errors, the measured data are not consistent with the $\sin^2\Theta_\phi^K$ distribution. The solid curve is a fit to the data with Eq. (12), from which the spin density matrix element $\rho_{00} = 0.23 \pm 0.04$ is determined. The deviation of ρ_{00} from the threshold value, together with the result presented in Eq. (11) and the lower frame of Fig. 9, indicates a significant admixture of $^3P_{1,2}$ partial waves in the outgoing protons for ϕ meson production at this beam momentum. ($^3P_0$ is forbidden in conjunction with $l_2 = 0$, since it would require a 1^+ pp entrance channel.)

Although the angular distribution shown in Fig. 11 deviates from isotropy, the deviation is sufficiently small that it justifies as a reasonable approximation the neglect of Θ_ϕ^K in acceptance matrix B, used for the total cross section determination.

IV. DISCUSSION

The ratio of the measured total cross sections for the $pp \to pp\phi$ and $pp \to pp\omega$ reactions presented in this report is plotted as the filled square in Fig. 12 in comparison to the other existing data at higher energies [40–43]. This data point is lower than the other data at higher energy. This is primarily due to the different mass of the ϕ and ω mesons, and the thereby ensuing strong variation of the ratio of available three body phase space volume near the ϕ meson threshold. These data are compared to a prediction based on a naive application of the OZI rule, including the variation of the available phase space (dashed curve). The data point from this measurement is enhanced by roughly one order of magnitude relative to the OZI prediction corrected for the available phase space volume.

The ϕ/ω ratio presented here is based on cross sections measured at the same beam momentum. In order to reduce uncertainty related to the different phase space volumes, par-
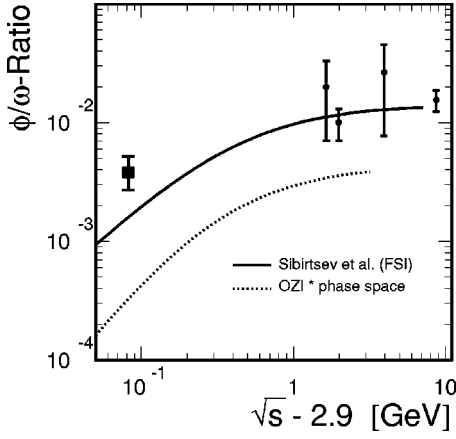
FIG. 12. Ratio of the total cross sections for the $pp\phi$ and $pp\omega$ reactions as a function of the c.m. energy above the ϕ production threshold. Shown is the value measured in this work (square) together with data at higher energies and model calculations described in the text.

tial wave amplitudes, and proton-proton final state interactions, it is useful to compare the ϕ/ω cross section ratio at the same c.m. energy above threshold. An evaluation based on the solid curve in the lower frame of Fig. 5 indicates that the cross section for the $pp \rightarrow pp\omega$ reaction is about 8.5 μb at the same c.m. energy above threshold as for the ϕ meson in this measurement (i.e., $Q = 83$ MeV). In this case the ϕ/ω ratio would only be enhanced by about a factor 5 relative to the OZI rule, in agreement with the higher energy data.

The solid curve in Fig. 12 is a calculation from Sibirtsev *et al.* [18] using a one pion exchange model and including the proton-proton final state interaction. These calculations, which describe the higher energy data well, have an energy dependence similar to the ratio of available phase space, and underestimate our point by about a factor of three. Using $\pi - N$ data, Sibirtsev [67] extracts a ratio of the transition amplitudes for $pp\omega$ to $pp\phi$ production $R = |M_\omega|/|M_\phi| = 8.5 \pm 1.0$. Assuming that R is independent of $\sqrt{s}$ near threshold, this calculation predicts the ϕ meson cross section to be (77 ± 16) nb at $Q = 83$ MeV. A similar model by Chung *et al.* [70] including off-shell features of the pion and interference between the direct and exchange diagrams predicts about 30 nb at this beam momentum. After applying the rather uncertain absolute normalization to our data (see Sec. II D), these predictions can be compared to our measured value of $190 \pm 14 \pm 80$ nb.

Another approach by Nakayama *et al.* [17] explicitly includes not only the mesonic current due to the $\pi\rho \rightarrow \phi$ coupling, but also the nucleonic current where the ϕ meson couples directly to the nucleon. The observed angular distribution, which is nearly isotropic, indicates a dominance of the mesonic current in contrast to the $\cos^2\Theta^\phi_{c.m.}$ distribution expected for the nucleonic current. As a result of the dominance of the mesonic current, they can not extract a unique value for the coupling constant $g_{NN\phi}$. In a similar model by Titov *et al.* [19,71], our total cross section and differential cross section as a function of $\Theta^\phi_{c.m.}$ can also be reproduced

without requiring an enhancement of $g_{\phi NN}$ over the OZI rule prediction. The importance of the correlated $\pi - \rho$ coupling, and the small value of $g_{NN\phi}$ have both been predicted by Meißner *et al.* [15] to result from large cancellations between intermediate kaon and hyperon graphs.

Although the value of $g_{\phi NN}$ is only poorly determined at this point, due to uncertainties in the calculations it appears as though our measured data can be explained without invoking a large explicit violation of the OZI rule. Nevertheless, the large decay width $\Gamma_{\phi \rightarrow \pi\rho}$ violates the OZI rule itself and requires kaon loop diagrams for a quantitative explanation [72]. Thus, all these solutions require a dominant role of intermediate states with open strangeness, thereby indicating that there must indeed be a significant amount of strange sea quarks available in reactions involving protons.

Ellis *et al.* claim that the enhanced ϕ meson production observed in $\bar{p}p$ reactions proceeds dominantly through the "rearrangement" process [11]. To a large degree this is based on the observation that the enhanced ϕ yield is strongly correlated to the initial spin triplet state in $p\bar{p}$ annihilation [38]. Recent results on $\bar{n}p$ annihilation in flight [73] and $\bar{p}d$ Pontecorvo reactions [74] support this hypothesis. According to their model, the "shake-out" process should not depend upon the initial spin state, and the "rearrangement" process should dominantly occur in the spin triplet state for polarized strange sea quarks, in agreement with the data. Following this argumentation, ϕ meson production in proton-proton reactions is also expected to be strongly correlated with the spin triplet initial state.

Directly at threshold, the proton-proton entrance channel must be in a $^3P_1$ state due to parity and angular momentum conservation, and consequently, the spin of the ϕ meson is aligned along the beam axis. At $Q = 83$ MeV we observe the spin density matrix element ρ_{00} to have a large deviation from the threshold prediction. This deviation is in qualitative agreement with the dilution of the spin alignment expected due to the observed contribution of the $l_1 = 1$ partial wave in the exit channel, and suggests that a significant fraction of the ϕ meson production at this beam momentum proceeds via the spin singlet $^1S_0$ and $^1D_2$ entrance channels.

TABLE VI. Differential cross sections for ω (left two columns) and ϕ (right two columns) meson production as functions of $\cos(\Theta^\omega_{c.m.})$ and $\cos(\Theta^\phi_{c.m.})$, respectively.

$\cos(\Theta^\omega_{c.m.})$	$d\sigma/d\Omega$ [μb/sr]	$\cos(\Theta^\phi_{c.m.})$	$d\sigma/d\Omega$ [nb/sr]
-0.9		-0.9	8.6 ± 29.5
-0.7	3.5 ± 2.0	-0.7	15.3 ± 4.5
-0.5	3.3 ± 0.4	-0.5	17.4 ± 3.3
-0.3	2.9 ± 0.34	-0.3	16.6 ± 2.0
-0.1	3.0 ± 0.29	-0.1	17.2 ± 2.0
0.1	3.1 ± 0.23	0.1	13.3 ± 1.5
0.3	2.9 ± 0.13	0.3	16.6 ± 1.4
0.5	3.3 ± 0.07	0.5	14.5 ± 1.2
0.7	3.9 ± 0.09	0.7	15.4 ± 1.2
0.85	5.4 ± 0.1	0.9	16.2 ± 1.2
0.95	8.0 ± 0.1		

TABLE VII. Differential cross sections for the $pp \to pp\phi$ reaction as a function of the angle of a proton measured in the pp reference frame relative to the beam direction (left two columns) and relative to the direction of the ϕ meson (center two columns). The right two columns tabulate the differential cross section as a function of the polar angle of the daughter K^+ meson, measured in the ϕ meson reference frame, relative to the beam direction.

$\cos(\Theta_{pp}^p)$	$d\sigma/d\Omega$ [nb/sr]	$\cos(\Psi_{pp}^p)$	$d\sigma/d\Omega$ [nb/sr]	$\cos(\Theta_\phi^{K^+})$	$d\sigma/d\Omega$ [nb/sr]
−0.875	15.4±2.5	−0.875	18.7±2.7	−0.875	10.3±2.4
−0.625	16.2±1.7	−0.625	17.1±3.8	−0.625	15.5±1.6
−0.375	15.3±1.9	−0.375	14.2±2.8	−0.375	16.4±1.7
−0.125	14.8±1.8	−0.125	11.8±2.4	−0.125	17.4±1.3
0.125	15.9±1.9	0.125	12.2±1.9	0.125	17.6±1.6
0.375	14.1±1.6	0.375	14.4±2.2	0.375	15.0±2.0
0.625	15.8±1.8	0.625	14.5±2.4	0.625	16.2±1.8
0.875	13.5±1.5	0.875	18.0±2.9	0.875	12.6±2.7

V. SUMMARY AND CONCLUSIONS

In this paper total and differential cross section values for the production of ϕ and ω mesons in proton-proton reactions at 3.67 GeV/c are presented. The total cross section ratio for these mesons is observed to be about an order of magnitude larger than expected from predictions based on a naive application of the OZI rule. This enhancement is slightly larger than the data measured at higher beam momenta, however significant uncertainty remains regarding the relative contributions of different partial waves to the ϕ versus ω production processes.

Apparent violations of the OZI rule in $\bar{p}p$ reactions have sometimes been attributed to a significant contribution of intrinsic strangeness to the proton's wave function. On the other hand, most of the observed enhancement of the ϕ meson yield in $\bar{p}p$ annihilation can be explained in terms of rescattering and loop diagrams. However, the large $\phi \to \pi\rho$ coupling also requires kaon loops, and thus the intermediate states are dominated by hadrons with strange quark content. Therefore, both interpretations involve a significant contribution of strange sea quarks to hadronic reactions involving protons.

Further information to help determine the origin of the strange sea quarks can be taken from polarization observables. For instance, based on a dominance of the rearrangement process, the polarized intrinsic strange sea quarks prefer a spin triplet initial state for ϕ meson production. The differential cross sections presented in this report indicate that the proton-proton entrance channel is not in a pure $^3P_1$ state at the beam momentum of 3.67 GeV/c. If the polarized intrinsic strangeness model is correct, then the ϕ/ω ratio should increase in direct proportion to the fraction of spin triplet in the initial state. Thus, it would be very useful to follow the correlation of the ϕ/ω ratio to the spin triplet fraction as a function of beam momentum closer to threshold where the triplet fraction must rise.

Another sensitive test of the intrinsic strangeness model would be to determine the ϕ meson production cross section in proton-neutron reactions. For instance, based on the intrinsic strangeness model, Ellis *et al.* predict the cross section ratio to be $\sigma_{np \to np\phi}/\sigma_{pp \to pp\phi} \approx 0.25$ near threshold [11]. In contrast, meson exchange models [19,68] predict $\sigma_{np \to np\phi}/\sigma_{pp \to pp\phi} \approx 5$ near threshold.

Finally, it would also be very important to determine the

TABLE VIII. Differential cross sections for the $pp \to pp\phi$ reaction as a function of the c.m. momentum of the ϕ meson (q, left two columns) and as a function of the proton momentum in the proton-proton reference frame (p, right two columns).

q [GeV/c]	$d\sigma/dq$ [μb/(GeV/c)]	p [GeV/c]	$d\sigma/dp$ [μb/(GeV/c)]
0.017	0.011±0.012	0.0145	0.0±0.55
0.051	0.064±0.015	0.0435	0.079±0.040
0.085	0.180±0.030	0.0725	0.178±0.037
0.119	0.379±0.038	0.1015	0.199±0.060
0.153	0.573±0.052	0.1305	0.457±0.058
0.187	0.680±0.078	0.1595	0.819±0.087
0.221	0.923±0.097	0.1885	0.961±0.083
0.255	1.09±0.087	0.2175	1.25±0.12
0.289	0.955±0.11	0.2465	1.30±0.11
0.323	0.585±0.083	0.2755	0.926±0.087
0.357	0.148±0.098	0.3045	0.382±0.065

ω meson yield and partial wave contributions at the same excess energy relative to the threshold as presented here for the φ meson. The angular distributions closer to threshold are needed to disentangle the mechanisms involved in the ω meson production [75], and this would eliminate the uncertainty related to the relative contributions of the different partial waves in the $pp\omega$ and $pp\phi$ systems.

ACKNOWLEDGMENTS

APPENDIX: DATA TABLES

In this section the differential cross sections presented in the figures above are listed in Tables VI, VII, and VIII. In addition to the statistical errors quoted here, there are the systematic errors and the overall normalization uncertainty discussed above.

[1] Particle Data Group, C. Caso *et al.*, Eur. Phys. J. C **3**, 1 (1998).

[2] G. Zweig, CERN Report No. 8419/th (1964), p. 412.

[3] S. Okubo, Phys. Lett. **5B**, 165 (1965).

[4] I. Iizuka, Suppl. Prog. Theor. Phys. **37-38**, 21 (1966).

[5] S. Okubo, Phys. Rev. D **16**, 2336 (1977).

[6] H.J. Lipkin, Phys. Lett. **60B**, 371 (1976).

[7] J. Ellis, M. Karliner, D.E. Kharzeev, and M.G. Sapozhnikov, Phys. Lett. B **353**, 319 (1995).

[8] J. Reifenrother *et al.*, Phys. Lett. B **267**, 299 (1991).

[9] V.G. Ableev *et al.*, Phys. Lett. B **334**, 237 (1994).

[10] C. Amsler *et al.*, Phys. Lett. B **346**, 363 (1995).

[11] J. Ellis, M. Karliner, D.E. Kharzeev, and M.G. Sapozhnikov, Nucl. Phys. **A673**, 256 (2000).

[12] S.J. Brodsky and B.-Q. Ma, Phys. Lett. B **381**, 317 (1996).

[13] M. Burkardt and B.J. Warr, Phys. Rev. D **45**, 958 (1992).

[14] H.J. Lipkin, Nucl. Phys. **B244**, 147 (1984).

[15] Ulf-G. Meißner, V. Mull, J. Speth, and J.W. Van Orden, Phys. Lett. B **408**, 391 (1997).

[16] V.E. Markushin, Nucl. Phys. **A655**, 185 (1999).

[17] K. Nakayama, J.W. Durso, J. Haidenbauer, C. Hanhart, and J. Speth, Phys. Rev. C **60**, 055209 (1999).

[18] A. Sibirtsev, Nucl. Phys. **A604**, 455 (1996); (private communication).

[19] A.I. Titov, B. Kämpfer, and V.V. Shklyar, Phys. Rev. C **59**, 999 (1999).

[20] K.A. Aniol *et al.*, Phys. Rev. Lett. **82**, 1096 (1999).

[21] D.T. Spayde *et al.*, Phys. Rev. Lett. **84**, 1106 (2000).

[22] H.W. Hammer and M.J. Ramsey-Musolf, Phys. Rev. C **60**, 045205 (1999).

[23] J. Ashman *et al.*, Phys. Lett. B **206**, 364 (1988).

[24] J. Ashman *et al.*, Nucl. Phys. **B328**, 1 (1998).

[25] P. Amandruz *et al.*, Phys. Lett. B **295**, 159 (1992).

[26] P.L. Anthony *et al.*, Phys. Rev. Lett. **71**, 959 (1993).

[27] K. Abe *et al.*, Phys. Lett. B **404**, 377 (1997).

[28] D. Adams *et al.*, Phys. Lett. B **357**, 248 (1995).

[29] K. Abe *et al.*, Phys. Lett. B **442**, 484 (1997).

[30] D. Adams *et al.*, Phys. Rev. D **56**, 5330 (1997).

[31] A. Airapetian *et al.*, Phys. Lett. B **442**, 484 (1998).

[32] B. Adeva *et al.*, Phys. Lett. B **420**, 180 (1998).

[33] K. Ackersdorf *et al.*, Phys. Lett. B **464**, 123 (1999).

[34] T.P. Cheng and R.F. Dashen, Phys. Rev. Lett. **26**, 594 (1971).

[35] T.P. Cheng, Phys. Rev. D **13**, 2161 (1976).

[36] J. Gasser, H. Leutwyler, M.P. Locher, and M.E. Sanio, Phys. Lett. B **213**, 85 (1988).

[37] J. Gasser, H. Leutwyler, and M.E. Sainio, Phys. Lett. B **253**, 252 (1991).

[38] A.M. Bertin *et al.*, Phys. Lett. B **388**, 450 (1996).

[39] F. Balestra *et al.*, Nucl. Instrum. Methods Phys. Res. A **426**, 385 (1999).

[40] V. Blobel, H. Fesefeldt, H. Franz, A. Hoffman, Ch. Jetter, H. Neumann, B. Schroder, and P. Soding, Phys. Lett. **59B**, 88 (1975).

[41] R. Baldi, T. Böhringer, P.A. Dorsaz, V. Hangerbühler, M. W. Kienle-Focacci, M. Martin, A. Mermond, C. Nef, and P. Segrist, Phys. Lett. **68B**, 381 (1977).

[42] M.W. Arenton, D.S. Ayres, R, Diebold, E.N. May, L. Nodulman, J.R. Sauer, C. Sorensen, A.B. Wicklund, and E.C. Swallow, Phys. Rev. D **25**, 2241 (1982).

[43] S.V. Golovkin *et al.*, Z. Phys. A **359**, 435 (1997).

[44] F. Balestra *et al.*, Phys. Rev. Lett. **81**, 4572 (1998).

[45] F. Balestra *et al.*, Phys. Lett. B **468**, 7 (1999).

[46] P. Lichard, Phys. Rev. D **49**, 5812 (1994).

[47] M. Stevenson *et al.*, Phys. Rev. **125**, 687 (1962).

[48] P. Weidenaur *et al.*, Z. Phys. C **59**, 387 (1993).

[49] A. Abele *et al.*, Phys. Lett. B **417**, 197 (1998).

[50] C. Amsler *et al.*, Phys. Lett. B **346**, 203 (1995).

[51] J.G. Layter, J.A. Appel, A. Kotlewski, W. Lee, S. Stein, and J.J. Thaler, Phys. Rev. D **7**, 2565 (1973).

[52] J. Smyrski *et al.*, Phys. Lett. B **474**, 182 (2000).

[53] H. Calén *et al.*, Phys. Lett. B **366**, 39 (1996).

[54] A.M. Bergdolt *et al.*, Phys. Rev. D **48**, R2969 (1993).

[55] E. Chiavassa *et al.*, Phys. Lett. B **322**, 270 (1994).

[56] E. Pickup, D.K. Robinson, and E.O. Salant, Phys. Rev. Lett. **8**, 329 (1962).

[57] G. Alexander, O. Benary, G. Czapek, B. Haper, N. Kidron, B. Reuter, A. Shapira, E. Simopoulou, and G. Yekutieli, Phys. Rev. **154**, 1284 (1967).

[58] L. Bodini *et al.*, Nuovo Cimento A **58**, 475 (1968).

[59] A.P. Colleraine and U. Nauenberg, Phys. Rev. **161**, 1387 (1967).

[60] C. Caso *et al.*, Nuovo Cimento A **55**, 66 (1968).

[61] E. Colton and E. Gellert, Phys. Rev. D **1**, 1979 (1970).

[62] G. Yekutieli *et al.*, Nucl. Phys. **B18**, 301 (1970).

[63] S.P. Almeida *et al.*, Phys. Rev. **174**, 1638 (1968).

[64] T. Vetter, A. Engel, T. Biró, and U. Mosel, Phys. Lett. B **263**, 153 (1991).

[65] F. Hibou *et al.*, Phys. Rev. Lett. **83**, 492 (1999).

[66] A. Sibirtsev and W. Cassing, Few-Body Syst., Suppl. **99**, 1 (2000).

[67] A. Sibirtsev and W. Cassing, Eur. Phys. J. A **7**, 407 (2000).

[68] M.P. Rekalo, J. Arvieux, and E. Tomasi-Gustafsson, Z. Phys. A **357**, 133 (1997).

[69] R.G. Newton, *Scattering Theory of Waves and Particles* (Springer-Verlag, New York, 1982).

[70] W.S. Chung, G.Q. Li, and C.M. Ko, Nucl. Phys. **A625**, 347 (1997).

[71] A.I. Titov, B. Kämpfer, and B.L. Reznik, Eur. Phys. J. A **7**, 543 (2000).

[72] V.E. Markushin, Nucl. Phys. B (Proc. Suppl.) **56A**, 303 (1997).

[73] A. Filippi *et al.*, Nucl. Phys. **A655**, 453 (1999).

[74] A. Abele *et al.*, Phys. Lett. B **469**, 276 (1999).

[75] K. Nakayama, A. Szczurek, C. Hanhart, J. Haidenbauer, and J. Speth, Phys. Rev. C **57**, 1580 (1998).